Searching for gravitational waves with eccentricity from compact binary coalescences

Author: Elwin K. Y. Li[a],

Mentor: Alan J. Weinstein[b]

Hong Kong University of Science and Technology, Clear Water Bay, Kowloon, Hong Kong[a]

LIGO Laboratory, California Institute of Technology, Pasadena, CA 91125, USA[b]

Email: kyeliaa@connect.ust.hk[a], ajw@caltech.edu[b]

(Dated: November 10, 2023)

Gravitational waves (GWs)[1, 2] are fundamental predictions of the General Theory of Relativity (GR). GWs detections have introduced a novel window into the universe and are revolutionizing our understanding of astrophysics. The motion of two massive objects in an eccentric orbit emits GWs which carry information about the eccentricity of the binary black hole (BBH) source. These waveforms are characterized by their eccentricity, which measures the deviation of the orbit from a quasi-circular orbit. Studying eccentric binary orbits provides evidence for the dynamic formation of the binary system. In this project, we study a new family of GWs waveforms from eccentric binaries and their implications for detecting and analyzing eccentric compact binary systems near mergers. We develop eccentric waveform models and parameter estimation frameworks for eccentric BBH and use these tools to analyze the data from current and upcoming GWs observations. Since eccentric waveforms are predicted to have similar waveforms with GWs from BBH systems with spin precession, we study how well we can distinguish eccentric waveforms and precessing waveforms by investigating their differences. We will determine the minimum eccentricity that could be detectable with GWs as a function of SNR and other parameters.

I. INTRODUCTION AND MOTIVATION

A. Background

The discovery of GWs, initially proposed by GR[3–6], has brought a new observational window on the cosmos. Exploring the properties of GWs can provide us with fresh perspectives into the properties of massive compact objects (neutron stars and black holes) in the universe and their role in the evolution of galaxies.

B. Gravitational Waves

GWs are ripples in space-time, which propagate outward at the speed of light, generated by the acceleration of massive objects. BBH mergers and binary neutron star (BNS) mergers are compact binary coalescences (CBCs) that generate detectable gravitational waves. Since the distance of CBCs from Earth is extremely far, GWs generated are extremely weak and hard to detect when they reach the Earth. They were first predicted in 1916 by GR. GWs have a property called polarization, which describes the orientation of the ripples. Just as electromagnetic waves have different polarizations (linear, circular, or elliptical), GWs can also have different polarizations. GWs have two transverse polarization modes: plus-polarization (h_+) and cross-polarization (h_+). The terms plus and the cross will be collectively known as the polarization basis. They stretch and compress the space-time in the two directions orthogonal to the direction of propagation[7]. h_+ describes the stretching and squeezing of space in one direction transverse to the direction of propagation. The impact on test particles in a $h_\times$ GWs would be similar to that of $h_\times$ polarized GWs but with a 45-degree rotation.

C. Gravitational Wave Detectors

Nowadays, gravitational waves can be detected by gravitational waves observatories[8], including Advanced LIGO (aLIGO)[9], VIRGO[10], and Kagra[11], which already have conducted three observing runs[12–14] in total. Figure 1 shows the configuration of the laser interferometer at the heart of the LIGO detectors and the laser mirrors (test masses) on their quadruple-pendulum suspensions. Since the two arms have the same nominal length, the split laser beams will have destructive interference at the output port when joined at the beam splitter, and the detector will register no signal. When GWs pass through the detector, the arms will be stretched or compressed differentially, resulting in length differences. The interference pattern will then be partially constructive such that a weak signal can be detected at the output port.
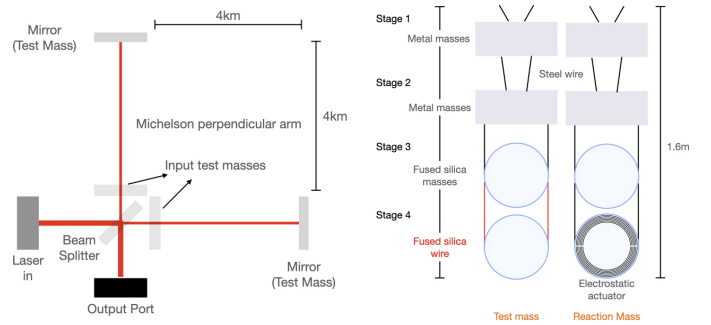

Figure 1. Interferometer configuration (Left) and test mass setup (Right).

D. Eccentric Binaries

When two massive objects move in an eccentric orbit, they generate GWs waveforms that encode the eccentricity - eccentric waveforms. The eccentricity of these waveforms reflects the extent of orbit deviation from a quasi-circular inspiralling orbit. For a quasi-circular orbit (since eccentricity = 0), there are fifteen parameters (plus one or more tidal parameters for BNS) to determine GWs, including the masses of the two mergers, the spin of the two mergers in three different directions (x, y, and z directions for both compact objects), source distance, sky location (right ascension and declination), coalescence time, coalescence phase, inclination and polarization, eccentricity is not one of the parameters. Since GWs are dominantly quadrupolar radiation, the frequencies of GWs (f_{GW}) are double that of the orbital frequencies (f_{orb}). Our detectors cannot detect GWs when f_{GW} is lower than 20Hz. The orbit might be eccentric at $f_{GW} = 20$Hz but become less eccentric or quasi-circular when the two sources are getting close with the gravitational wave frequency higher than 20Hz. If the eccentricity is high at $f_{GW} = 20$Hz, it is predicted to approach zero by the time $f_{GW} = 50$Hz.

In GWs astrophysics, it is important to investigate eccentric gravitational waveforms as they can offer valuable information about the formation characteristics of BBH. Several studies[15, 16] have been conducted on eccentric gravitational waveforms based on the standard approach and a novel method suggested[17], which uses parameter estimation. These investigations offer new perspectives into the characteristics of these waveforms and their possible uses in examining the cosmos.

E. BBH Formation in Isolation and Dynamical Capture

BBHs are common in the universe. BBH systems may form through common evolution in isolation (first column of Fig 2). Another possibility is dynamical capture, in which the binary system is formed by capturing other massive objects (second column in Fig. 2). Other formation mechanisms are predicted as well. We do not know which of these formation mechanisms are dominant for systems that merge in the LIGO frequency band.

One of our primary goals is to understand how compact binary systems form. One possibility is the BBH Formation in Isolation, in which a binary system evolves together, undergoes Roche lobe overflow and a common envelope stage that tightens the binary orbit through dynamical friction. One of the stars will directly turn into a black hole. If a common envelope occurs, the giant envelope will surround the orbit of the system. Thermal energy is transferred to the envelope and may trigger the ejection of the envelope. Once the ejection of the envelope occurs, the massive star will directly turn into a black hole, leading to the inspiral of the two black holes and merging into a single one at the end. This BBH formation

and merger is a common evolution in which the eccentricity has radiated away by the time the GWs reach the LIGO band. Another possibility is BBH formation in dense star clusters (e.g., at the center of galaxies or in globular clusters) through dynamical capture. The binary massive star system undergoes a similar process as the BBH formation in isolation unless another massive BH is captured by the cross-section area of the two stars, ejecting the massive stars out of the original orbit and forming a new BBH system.[18] Since the new-coming BH removed some orbital energy from the initial orbit, the orbit is closer to merger and highly eccentric. This process is called dynamical capture. The probability of dynamicql capture is related to the capture cross-section. Another scenario of BBH Formation by dynamical capture is when a fast-moving BH loses kinetic energy through gravitational radiation and is then captured by another BH. Figure 2 shows the evolution of the three BBH formation mechanisms. These are three of the many examples of BBH formation. Other examples also exist (including hierarchical mergers) and contribute to BBH capture or formation. The study of eccentric GWs provides valuable information to determine which form of BBH formation dominates. We also want to look for dynamic capture with a very small cross-section such that the time to the merger is within seconds.
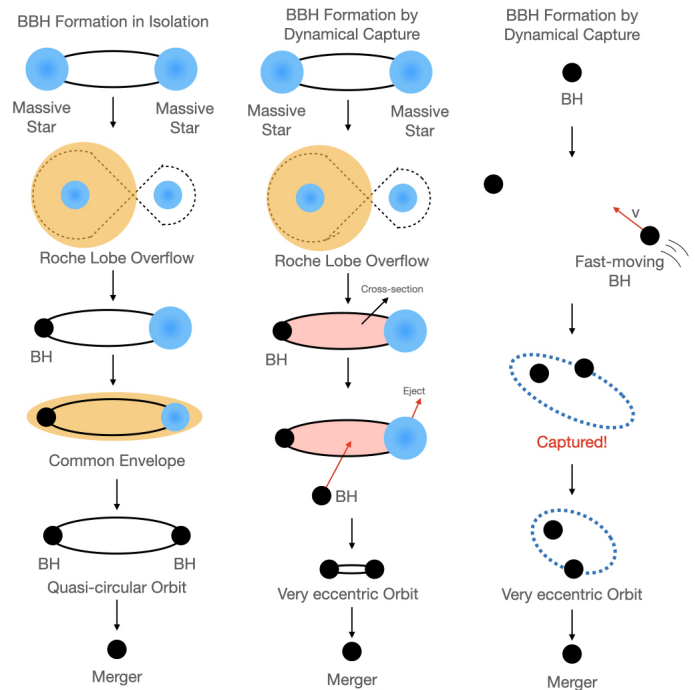

Figure 2. Following Michela Mapelli et al., BBH Formation in Isolation (Left) and by Dynamical Capture (Right)[18]. Another scenario of BBH Formation by Dynamical Capture (Middle).

F. Matched-filtering

Matched-filtering[19], implemented (for example) in the PyCBC[20–22] search pipeline, is a technique that can detect

numerous possible GWs candidates from a given period with similar shapes. It can detect signals from stationary Gaussian noise by sliding the template waveforms across the data and calculating the SNR, as shown in Figure 3. The match between two signals can be calculated by performing waveform overlap using matched-filtering.
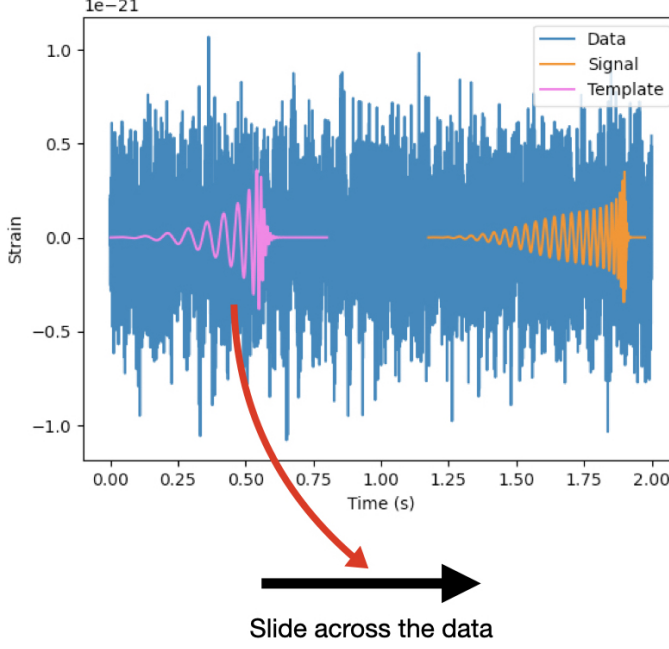

Figure 3. A figure visualizing the process of matched-filtering.

Suppose $n(t)$ is the stationary Gaussian noise process, $S_n(f)$ is the one-sided power spectral density (PSD) given by

$$\langle \tilde{n}(f)\tilde{n}^*(f') \rangle = \frac{1}{2}S_n(|f|)\delta(f - f'), \tag{1}$$

the matched-filtering output of a data stream is

$$x(t_0) = 2\int_{-\infty}^{\infty} \frac{\tilde{s}(f)\tilde{h}^*_{template}(f)}{S_n(f)}df \tag{2}$$

which may only contain noise $s(t) = n(t)$, or signal with noise $s(t) = n(t) + h(t)$ where $h(t)$ is the signal. Denote $h_{template}(t)$ as the filter template. Since there are unknown parameters (amplitude, coalescence phase, and binary companion masses) in the waveform, the "best match" unknown phase ϕ_0 has to be found by maximizing $x(t_0)$ over ϕ_0. $x(t_0)$ is defined as

$$x(t_0) = x_{re}(t_0)cos2\phi_0 + x_{im}(t_0)sin2\phi_0, \tag{3}$$

where $x_{re,im}$ can be found by using Eq. 2 with $\phi_0 = 0$. Therefore, the maximum value can be found using the equation

$$x^2(t_0)|_{\hat{\phi}_0 maximum} = x^2_{re}(t_0) + x^2_{i,i}(t_0) \tag{4}$$

at $2\hat{\phi}_0 = arg(x_{re} + ix_{im})$. The modulus of complex filter output then gives the maximum:

$$z(t_0) = x_{re}(t_0) + ix_{im}(t_0) \tag{5}$$

$$= 4\mathbb{R}\int_0^{\infty} \frac{\tilde{s}(f)(\tilde{h}^*_{template}(f))_0}{S_n(f)}e^{2\pi i f t_0}df, \tag{6}$$

where $(\tilde{h}^*_{template}(f))_0 = (\tilde{h}^*_{template}(f))_{t_0=0,\phi_0=0}$. The normalization constant for each template is calculated by

$$\sigma_m^2 = 4\int_0^{\infty} \frac{|\tilde{h}_{1Mpc,m}(f)|^2}{S_n(f)}df, \tag{7}$$

such that the Signal-to-Noise Ratio (SNR) can be calculated afterward. The amplitude SNR of the quadrature matched-filtering is given by

$$\rho_m(t) = \frac{|z_m(t)|}{\sigma_m}. \tag{8}$$

If the signal is absent, then

$$< \rho_m^2 > = 2. \tag{9}$$

Since for purely static and Gaussian noise, obtaining $\rho_m >> 1$ is improbable, a threshold, such as $\rho_m > 4$, is often used to identify event candidates.

In the presence of non-Gaussian excess noise, search pipelines such as PyCBC introduce an SNR Likelihood Ratio $\mathcal{L}$, a detection statistic used to identify and rank event candidates. For each trigger, a False-Alarm-Probability (FAP), which is the probability that noise can produce a trigger with a ranking statistic $\ln \mathcal{L} \geq \ln \mathcal{L}^*$, is calculated as

$$\textbf{FAP} = P(\ln \mathcal{L} > \ln \mathcal{L}^*|\textbf{noise}) = \int_{\ln \mathcal{L}^*}^{\infty} P(\ln \mathcal{L}|\textbf{noise})d\ln \mathcal{L} \tag{10}$$

The lower the FAP, the more likely the trigger comes from an actual GWs signal.

G. Bilby and Parameter Estimation

Bilby[23], an interface for performing parameter estimation (PE)[24], aims to deduce parameters of CBC waveforms. It uses the Bilby Markov chain Monte Carlo (BILBY-MCMC)[25] or dynesty sampling algorithm to map out the possible parameters of the waveforms.

1. Bayes Formula and Probability Density Function

Bayes Formula represents a statistical equation to determine the likelihood of a particular event happening under specific conditions. The probability of an event A given a condition B is given by

$$P(A \mid B) = \frac{P(A \cap B)}{P(B)}. \tag{11}$$

The probability of B given A is given by

$$P(B \mid A) = \frac{P(B \cap A)}{P(A)} = \frac{P(A \cap B)}{P(A)}. \qquad (12)$$

By substituting Equation 12 into Equation 11, we get

$$P(A \mid B) = \frac{P(B \mid A)P(A)}{P(B)}, \qquad (13)$$

which is the Bayes Formula.

The probability Density Function (PDF), or the posterior probability, is the probability of an event given a condition. In GWs PE, it is used to find out the probability that the estimating parameters θ can describe the data d by

$$P(\theta \mid d) = \frac{P(d \mid \theta)P(\theta)}{P(d)}, \qquad (14)$$

where $P(d \mid \theta)$ is called the likelihood, $P(\theta)$ is called the prior, $P(d)$ is called the evidence. It is challenging to find the probability that θ can describe d in reality, but it is easy to find the probability that d can describe the data θ. One can calculate $P(\theta \mid d)$ using PDF to estimate the posterior probability distribution for the thetas

The likelihood is the probability of the data given a parameterized model of a signal presumed to be in the noisy data. In GWs PE, the likelihood $\mathcal{L}(d \mid \theta)$ is the probability of d with the given θ. For each frequency, $\mathcal{L}(d_i \mid \theta)$ is given by

$$\mathcal{L}(d_i \mid \theta) = \frac{2\Delta f}{\pi S_n(f_i)} \exp\left(-2\Delta f \frac{(d(f_i) - h(f_i, \theta))^2}{S_n(f_i)}\right), \qquad (15)$$

where $d(f_i)$ is the data time-series, Fourier transformed into the frequency domain, $h(f_i, \theta)$ is the signal, $d(f_i) - h(f_i, \theta)$ is the Gaussian noise for the best choice of parameters. The total $\mathcal{L}(d \mid \theta)$ is given by

$$\ln\left(\mathcal{L}(d \mid \theta)\right) = \sum_{i=1} \ln \mathcal{L}(d_i \mid \theta), \qquad (16)$$

The prior is the probability of the event without any new information.

The evidence is the integral of the numerator of Equation 14, which includes all of the information from the data. It is the evidence for the model, integrated over all possible values of the parameters as specified by the priors, weighted by the parameter likelihood. It turns the left-hand side of Equation 14 into a normalized posterior PDF. It is used to compare different models by Bayesian model selection.

2. Bilby Markov chain Monte Carlo Parameter Estimation

BILBY-MCMC algorithms use a sequential stepping process to generate correlated samples from the target distri-
bution. Specifically, applying the Metropolis-Hastings algorithm facilitates the production of samples from the target density. A random draw from the prior distribution $P(\theta)$ is utilized to initialize the chain, and then the Metropolis-Hastings algorithm is iterated to generate a chain θ_i containing m samples. Typically, these samples in the chain exhibit correlation by selecting a subset of $\frac{m}{\tau}$ samples, where τ is the auto-correlation time (ACT) of the chain. To obtain independent samples, one can select a subset by sampling every τ steps from the chain of samples. The algorithm is being iterated until the stopping criteria are reached. The stopping criteria are given by

$$n_{samples} \geq \frac{m - n_{burn}}{\gamma\tau}, \qquad (17)$$

where n_{burn} represents the number of samples discarded to eliminate the chain initialization, while $\gamma \leq 1$ denotes a thinning factor.

H. Likelihood Ratio and GWs Searching

The Likelihood, as defined above in Equation 15, is $\mathcal{L}(d \mid s + n)$, so the likelihood ratio is given by

$$\mathcal{L}_r = \frac{\mathcal{L}(d \mid s + n)}{\mathcal{L}(d \mid n)}, \qquad (18)$$

Here, n represents the statistical properties of the noise in the data, not the actual noise realization. Therefore, for noise only, $d - m$ is distributed as a Gaussian. $\mathcal{L}$ is the probability ratio of θ describing the (best-fit) signal to θ describing the residue after subtracting the signal from the data noise. The data likelihood ratio between the signal hypothesis and the noise hypothesis is then given by

$$\mathcal{L}(s \mid n) = \frac{\mathcal{L}(d \mid (n + s), t))}{\mathcal{L}(d \mid n)}. \qquad (19)$$

I. Rate of Change of Eccentricity

According to a pioneering study of GWs from CBCs[26], the time average of the rate of change of eccentricity of the orbit is given by:

$$\left\langle \frac{de}{dt} \right\rangle = -\frac{304 e G^3 m_1 m_2 (m_1 + m_2)}{15 c^5 a^4 (1 - e^2)^{5/2}} \left(1 + \frac{121e^2}{304}\right). \qquad (20)$$

Using this equation, we can evolve the eccentricity of eccentric BBH orbit as it inspirals and approaches merger.

II. OBJECTIVE

The research aims to evaluate the properties of existing and newly-developed GWs waveforms that incorporate the effects of non-zero eccentricity in the binary orbit. The result

of eccentricity on GWs waveforms and their detectability in LIGO has been shown in past studies[27],[28]. The existing data will be analyzed to compare eccentric and non-eccentric waveforms, and more detailed studies regarding this parameter will be conducted. This research will also analyze existing data and compare eccentric and non-eccentric waveforms to achieve these goals. This will provide insights into the effects of eccentricity on the waveform, which will then be used to conduct more in-depth studies on this parameter.

During the research period, eccentric waveforms, in addition to TEOBResumS, an eccentric waveform model which has not been used by LIGO, is being studied :

1. How does the eccentricity evolve with time as the binary system approaches merger?

2. Do the eccentric waveforms in the time and frequency domain generated by TEOBResumS pass a set of sanity checks that look reasonable and have proper limiting behavior?

3. How different or similar are eccentric waveforms generated by TEOBResumS and older waveform models that were constructed to describe eccentric binaries?

4. Can eccentric waveforms be distinguished from precessing waveforms?

5. Are eccentric waveforms detectable?

6. How can eccentric waveforms be identified with parameter estimation?

7. Implement TEOBResumS into Bilby to perform parameter estimation simulations.

8. Can eccentric waveforms be searched from LIGO data in previous observing runs?

9. How can eccentric waveforms be searched with parameter estimation?

Studying eccentricity in gravitational waveforms, regardless of its magnitude, is crucial as it can provide a more comprehensive understanding of the behavior of compact binary systems in a broader range of eccentricities. This research can shed light on the physics behind the inspiral and merger of binaries with higher eccentricities, which can lead to the detection of more GWs signals from such systems. Moreover, it can help improve our existing models for the dynamics of compact binaries, which can lead to more accurate parameter estimation and GWs detection. Studying high eccentricities can also help us understand the astrophysical processes responsible for producing such systems and their implications for cosmology and astrophysics. Therefore, this research can have a significant impact on understanding the universe and the properties of compact objects such as neutron stars and black holes.

III. METHODS

To conduct this study, simulated eccentric waveforms with different magnitudes of eccentricity were generated. To identify apparent differences, these waveforms will be compared to standard quasi-circular waveforms using matched-filtering and sanity checks. The study of eccentric waveforms involves using waveform overlap with standard waveforms. By comparing them, we can quantify the waveforms using parameter estimation, ensuring that eccentricity is considered when generating or detecting GWs signals.

The next step involves performing an injection study to simulate the GWs search process. GWs waveforms with random eccentricity were injected into random noise. It is first done by using PyCBC libraries and functions to test for the detectability of eccentric waveforms preliminarily. The simulation searched for the waveforms and find out the estimated eccentricity of the signal using Bilby.

The injection study will allow researchers to understand better the properties of eccentric waveforms and how they differ from regular waveforms. This information can then be used to improve the detection of GWs from eccentric sources, such as binary systems with large eccentricities.

After that, more parameters besides eccentricity will be randomized before injecting into random noise. BILBY-MCMC will be used to estimate all the unknown parameters of the injected waveforms. With sufficient testing and correct results, the simulation will be applied to actual data.

IV. PROCEDURES

Eccentric waveforms are the key to this research. Generally, there are three different major GWs models of waveforms, the post-Newtonian template[29], the SXS templates, and the recently developed templates that cover the full inspiral-merger-ringdowns and that explicitly incorporate both aligned spin and eccentricity; such as TEOBNRResumS_eccentric[30, 31]. Note that there currently are no waveform families in use by the LVK that incorporate both precessing spin and eccentricity. In the template bank of the post-Newtonian GWs model, eccentric waveforms generated do not contain merger and ringdown. TEOBResumS templates are new and are currently not used for data analysis in LIGO. However, eccentric waveforms from SXS are limited with fixed eccentricity and other parameters. To generate waveforms with variable eccentricities for my search, it is necessary to review the precision of the TEOBResumS templates.

A. Eccentricity Evolution Investigation

Equation 20 is only valid to the lowest post-Newtonian order, which is sufficient until late inspiral, close to the merger.

We use it here to simulate the early inspiral of a BBH system. The simulation shows that the higher the initial eccentricity, the smaller the inspiral time between them, as shown in Figure 4. Figure 5 also shows a similar result, with the y-axis being the orbital separation between the two BH. From Figure 6, with a high initial eccentricity of the orbit ($\varepsilon_0 = 0.9$), the orbital separation drops significantly when the $\varepsilon \geq 0.7$ and $\varepsilon \leq 0.1$. The orbital separation drops slowly when the eccentricity of the orbit is at the range $0.1 < \varepsilon < 0.7$. These plots indicate that it is possible to estimate the initial eccentricity ε_0 of the orbit when the eccentricity of the orbit at $f_{GW} = 20Hz$ is measured.

Figure 6. Change of orbital separation in the eccentricity of the orbit.

B. TEOBResumS Waveforms Model Reviewing Notebook

The review tests listed below are implemented in a series of Jupyter Python notebooks.

- Individual tests[1]

  - Test for the upper limit of eccentricity in which the waveform can be generated
  - Test for the behavior of the waveform with different eccentricities
  - Test for the total mass of the compact binaries to ensure the waveform varies smoothly
  - Test for the mass ratio of the compact binaries to ensure a smooth waveform can be generated
  - Test for the aligned spin of compact binaries to ensure a smooth waveform can be generated
  - Test for extreme cases of eccentricity, masses, and mass ratio

- Waveform Comparison and Matches[2,3]

  - Comparison between Eccentric TEOBResumS and Non-eccentric TEOBResumS waveforms
  - Comparison between Aligned-spin TEOBResumS and Eccentric TEOB waveforms
  - Comparison between Eccentric TEOBResumS and Eccentric SXS waveforms
  - Comparison between Eccentric TEOBResumS and Eccentric TaylorF2Ecc
  - Comparison between Eccentric TEOBResumS and Eccentric EccentricFD

Figure 4. Change of eccentricity of the orbit in time.
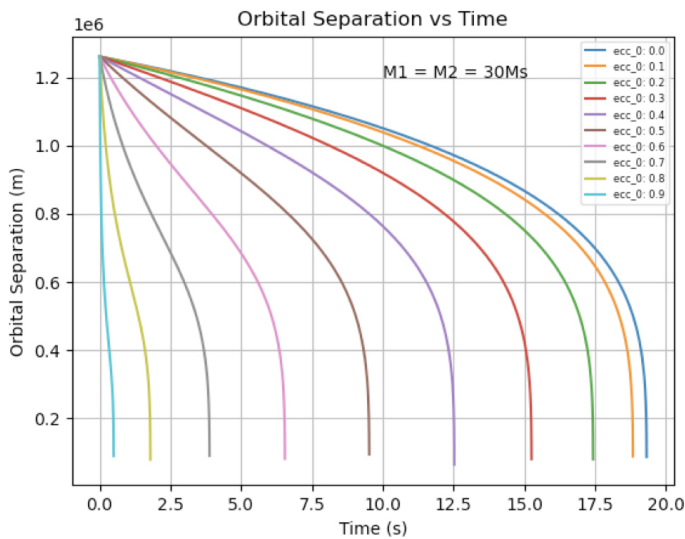
Figure 5. Change of orbital separation in time.

[1] Link to the Reviewing Notebook 1
[2] Link to the Reviewing Notebook 2
[3] Link to the Reviewing Notebook 3

– Comparison between align spin TEOBResumS and align spin IMRPhenomXPHM waveforms

– Comparison between Eccentric TEOBResumS and Precessing IMRPhenomXPHM waveforms

1. Test for the upper limit of eccentricity in which the waveform can be generated

Figure 7 shows that a GWs waveform with initial eccentricity $\varepsilon_0 = 0.99982$ at $f_{GW} = 20Hz$ gives a reasonable-looking waveform. However, the waveform becomes abnormal when the ε_0 reaches 0.99984, as shown in Figure 8. Therefore, we can conclude that the upper limit of eccentricity, which can be sensibly produced in the TEOBResumS model, is 0.99982. Waveforms with eccentricity higher than 0.99982 may fail.

2. Test for the behavior of the waveform with different eccentricities

By observing plots of the waveforms in the time domain with ε_0 from 0.0 to 0.9, the higher the eccentricity of the waveform, we see the oscillations collapse from sine waves into spikes. Figure 9 shows the waveforms in both the time and frequency domain. Waveforms with eccentricity fluctuate before the merger, with vigor depending on the eccentricity. Figure 10 shows how the sine wave collapses when ε_0 is high compared to when ε_0 is low.

3. Test for the total mass of the compact binaries to ensure the waveform varies smoothly

According to the plots, the waveform behaves reasonably to the eye. Figure 11 shows two plots with the waveforms with $\varepsilon_0 = 0.0$ and total mass from $10M_\odot$ to $100M_\odot$ and $110M_\odot$ to $200M_\odot$ in the time domain, while Figure 12 shows in the frequency domain. Figure 13 shows two plots with the waveforms with $\varepsilon_0 = 0.9$ and total mass from $10M_\odot$ to $100M_\odot$ and $110M_\odot$ to $200M_\odot$ in the time domain, while Figure 14 shows in the frequency domain.

The larger the total mass, the lower the frequency, right before the binary gets into a merger, which is expected. When the total mass is 800 solar masses, the binary is near the merger state when the GWs frequency is at 20Hz, which the complete waveform can hardly be detected with our current detectors. Figure 15 and Figure 16 show how the waveform when the total mass reaches the upper limit with $\varepsilon_0 = 0.0$ and $\varepsilon_0 = 0.9$, respectively. Therefore, we can conclude that the upper limit of the total mass for which the waveform exhibits oscillations at 20Hz or higher is $800M_\odot$.

4. Test for the mass ratio of the compact binaries to ensure a smooth waveform can be generated

According to the plots, the waveform behaves reasonably to the eye. Figure 17 shows two plots with the waveforms with $\varepsilon_0 = 0.0$ and mass ratio from 1 to 7 and 8 to 14 in the time domain, while Figure 18 shows in the frequency domain. Figure 19 shows two plots with the waveforms with $\varepsilon_0 = 0.9$ and mass ratio from 1 to 7 and 8 to 14 in the time domain, while Figure 20 shows in the frequency domain.

The plots also show that the waveform appears to behave sensibly. With no eccentricity, the mass ratio can be set to 10000. However, if the eccentricity of the waveform is 0.9, the waveform fails with a mass ratio of 1000. Figure 21 shows the waveform with $\varepsilon_0 = 0.0$ and mass ratio 1000, while Figure 22 shows that with $\varepsilon_0 = 0.9$ and mass ratio 100.

5. Test for the aligned spin of compact binaries to ensure a smooth waveform can be generated

According to the plots, TEOBResumS can generate aligned spin waveforms up to 1.0. Figure 23 shows two plots with the waveforms with $\varepsilon_0 = 0.0$ and spin from 0.0 to 0.5 and 0.6 to 1.0 in the time domain, while Figure 24 shows in the frequency domain. Figure 25 shows two plots with the waveforms with $\varepsilon_0 = 0.9$ and spin from 0.0 to 0.5 and 0.6 to 1.0 in the time domain, while Figure 26 shows in the frequency domain. From the plots, the waveforms vary smoothly and in a reasonable way. This suggests that the TEOBResumS can produce sensible waveforms, including both non-zero eccentricity and non-zero aligned spin.

6. Test for extreme cases for eccentricity, masses, mass ratio, and aligned spin

The extreme cases for maximizing the eccentricity, masses, mass ratio, and aligned spin are tested. By testing, the maximum combination is $\varepsilon_0 = 0.999$, total mass = $450M_\odot$, mass ratio = 45, and aligned spin = 1.0, as shown in Figure 27. Parameters higher than these values may lead to non-sensible waveforms.

C. Waveform Comparison and Matches

A simple matching model is being constructed to do waveform overlapping and match calculating between pairs of eccentric waveforms and non-eccentric waveforms and pairs of eccentric waveforms and precessing waveforms in both the time domain and frequency domain. The simulation uses waveforms with different eccentricities to overlap and calculate the match. After calculating the matches, graphs of the match, which are maximized over relative time and phase against the eccentricity of the testing waveform, are plotted.

1. Comparison between Eccentric TEOBResumS and Non-eccentric TEOBResumS waveforms

Figure 28 shows the waveforms of eccentric TEOBResumS with different ε_0 and non-eccentric TEOBResumS waveforms. Figure 29 and 30 shows the waveforms of eccentric TEOBResumS with $\varepsilon_0 = 0$ and non-eccentric TEOBResumS waveforms with mass ratio 1 and 15, respectively. The plots show that the eccentric TEOB waveform with $\varepsilon_0 = 0$ is precisely the same (match values are 1 in both time domain and frequency domain) as the non-eccentric TEOB waveform with mass ratios 1 and 15. This indicates the compatibility between eccentric TEOB and non-eccentric TEOB waveforms.

2. Comparison between Aligned-spin TEOBResumS and Eccentric TEOB waveforms

Figure 31 shows the waveforms of eccentric TEOBResumS with $\varepsilon_0 = 0.2$, and spin 1 and spin2 equal 0.2 in both the time and frequency domain. Figure 32 shows the waveforms of eccentric TEOBResumS with $\varepsilon_0 = 0.6$, and spin 1 and spin2 equal 0.6 in both the time and frequency domain. Figure 33 shows the waveforms of eccentric TEOBResumS with $\varepsilon_0 = 0.8$, and spin 1 and spin2 equal 1.0 in both the time and frequency domain. According to the plots, once the spin is added to the waveform, it differs from an eccentric waveform with a low match value between them. This demonstrates that an aligned-spin waveform is distinguishable from an eccentric waveform.

3. Comparison between Eccentric TEOBResumS and SXS waveforms

From the plots and calculated match values, most of the waveforms generated using TEOBResumS are highly similar to that from the SXS catalog (match value ≥ 0.85 in both time and frequency domains). This indicates the reliability of TEOBResumS waveforms with variable eccentricity values. Figure 34 compares BBH 1569 from the SXS catalog with $\varepsilon_0 = 1.341 \times 10^{-4}$ which is neglectable, and TEOB waveform with the same parameters as SXS in both the time and frequency domains. Figure 35 compares BBH 1373 from the SXS catalog with $\varepsilon_0 = 0.2087$ and TEOB waveform with the same parameters as SXS in both the time and frequency domains. Figure 36 compares BBH 1360 from the SXS catalog with $\varepsilon_0 = 0.3636$ and TEOB waveform with the same parameters as SXS in both the time and frequency domains.

4. Comparison between Eccentric TEOBResumS and Eccentric TaylorF2Ecc

From the plots, the TaylorF2Ecc waveforms have waveform modulations even when the eccentricity is zero, as shown in Figure 37. Figure 38 and Figure 39 show the comparisons between TaylorF2Ecc waveforms and TEOBResumS waveforms with an initial eccentricity of 0.5 and 0.9, respectively. Waveforms of TaylorF2Ecc also have unreasonable fluctuations at other eccentricities compared to TEOBResumS. According to the plots, TEOBResumS waveforms significantly differ from TaylorF2Ecc waveforms calculated from the Post-Newtonian method. In subsection 3 above, we consider that the SXS waveforms, computed directly with numerical relativity, are correct. Since TEOBResumS agrees well with the SXS waveforms but disagrees with the post-Newtonian TaylorF2Ecc waveforms, we conclude that the latter is unreliable.

5. Comparison between Eccentric TEOBResumS and Eccentric EccentricFD

From the plots, the EccentricFD waveforms have waveform modulations even when the eccentricity is zero, as shown in Figure 40. Figure 41 and Figure 42 show the comparisons between EccentricFD waveforms and TEOBResumS waveforms with an initial eccentricity of 0.5 and 0.9, respectively. Waveforms of it also have unreasonable fluctuations at other eccentricities compared to TEOBResumS. Similar to subsection 4 above, since TEOBResumS agrees well with the SXS waveforms but disagrees with the post-Newtonian TaylorF2Ecc waveforms, we conclude that the latter is unreliable.

6. Comparison between align spin TEOBResumS and align spin IMRPhenomXPHM waveforms both with zero eccentricity

From the plots, the aligned spin waveforms with zero eccentricity generated with TEOBResumS are nearly the same as those generated with IMRPhenomXPHM. Figures 43 to 45 show aligned-spin TEOB and aligned-spin IMRPhenomXPHM on the same graph with different values of aligned-spin in the time and frequency domains. This proves that the calculations in the aligned spin of the TEOBResumS waveform generator are accurate.

7. Comparison between Eccentric TEOBResumS and Precessing IMRPhenomXPHM waveforms

Observing the plots in the time domain shows that the amplitude modulation of precessing waveforms processes smoothly, while the amplitude of eccentric waveforms fluctuates vigorously before the merger. It would be hard to distinguish between precessing and non-precessing waveforms with zero eccentricity, as shown in Figure 46 and Figure 49. However, when eccentricity is significant, the match value between the precessing waveform and eccentric waveform will be lower than that of the precessing waveform and the non-precessing waveform with zero eccentricity. Figures 47, 48, and 50 compare eccentric waveforms with non-zero eccentricity generated by TEOBResumS and precessing waveforms generated by IMRPhenomXPHM. The higher the eccentricity, the lower the match between

the precessing waveform and the non-precessing waveform with zero eccentricity. This acts as evidence that waveforms from eccentric binaries can be distinguished from those from precessing binaries.

8. *Conclusions on review tests and comparisons*

By reviewing the TEOBResumS with a series of comparisons, it is concluded that TEOBResumS is a reliable waveform that can be added to the LIGO waveform model catalog.

D. Test for the Detectability of Eccentric Waveforms

The EcceNTric seaRch mOdel, also known as ENTRO, is constructed to test for the detectability of eccentric waveforms. ENTRO simulates actual scenarios by injecting eccentric waveforms with random eccentricity generated by TEOBResumS into a strain of random Gaussian noise using Py-CBC functions. By using matched-filtering, ENTRO recovers the eccentricity of the injected signal by comparing the SNR of different testing waveforms. The one with the highest SNR gives the best-recovered eccentricity value. Figure 51 and Figure 52 show the results of more than 9000 trial runs, with an average SNR of approximately 100 and 15, respectively. With a higher average SNR, ENTRO recovers the eccentricity of the injected signals more accurately, with an accuracy of more than 99.9%. More incorrect eccentricities are recovered with a lower average SNR, but it still achieves an accuracy of 95%. The blue outliers are rare cases where the underlying noise fluctuations confuse the recovery algorithm, and the algorithm itself is flawless. These prove the possibility of detecting eccentric waveforms in a strain of noise.

E. Bilby Implementation

As shown in Figure 52, when the SNR is low, which is expected, it is more difficult to recover the eccentricity of the GW signal by using ENTRO. To recover the eccentricity of the GWs in noises, the enhanced ENTRO, eENTRO, is constructed.

eENTRO is a simulation that recovers the eccentricity of the injected signal using Bilby. To do this, Bilby is taught to generate waveforms with eccentricity using the TEOBResumS model, as it is not included in Bilby. eENTRO is improved by performing PE using Bilby, which is a more accurate method to recover the eccentricity of the injected signal. Figure 53 and Figure 54 show the results of two trial runs with SNR of around 30. The eccentricity of the injected signal of the trial run shown in Figure 53 is 0.5, while the recovered eccentricity is 0.48694 with a precision of 97.4%. The eccentricity of the injected signal of the trial run shown in Figure 54 is 0.9, while that recovered by eENTRO is 0.899908 with

a precision higher than 99.9%. These results indicate the success of implementing the TEOBResumS model into Bilby, in addition to the feasibility of accurately recovering the eccentricity of GW signals in noise.

V. FUTURE PLANS

A. TEOBResumS Reviewing Notebook Optimization

After showing the notebooks to the LIGO Waveform Group and the TEOBResumS Group, it is suggested that the comparisons between waveforms generated by TEOBResumS and those by SXS could be much better, with a match of higher than 99%. Therefore, those comparisons will be further improved by changing the parameters used to generate waveforms using the TEOBResumS model.

B. eENTRO Optimization

eENTRO will be further optimized so that Bilby's results can always give accurate results of the recovered eccentricity. Other than eccentricity, other parameters, including the chirp mass of the orbit and the mass ratio of the BHs, will also be recovered by eENTRO to test for its comprehensiveness. Besides recovering only one parameter of the injected GW signals, a higher dimension search will be constructed to recover more parameters for each event.

C. Application of eENTRO

Once eENTRO is ensured to give accurate results, it will be upgraded to Parameter estimation EcceNTric seaRch mOdel, also known as PENTRO. PENTRO will construct parameter estimations on actual LIGO data. LIGO Livingston and LIGO Hanford will be taken into analysis.

VI. ACKNOWLEDGEMENT

VII. APPENDIX
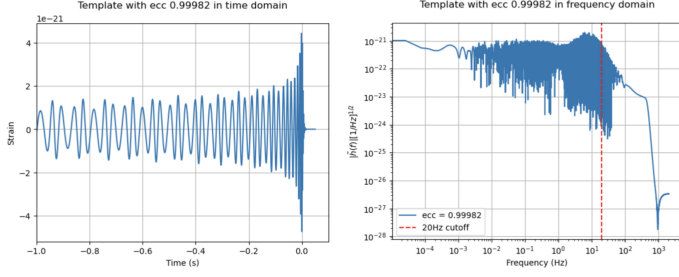
Figure 7. GWs waveform with $\varepsilon_0 = 0.99982$ in the time domain (left) and in the frequency domain (right).
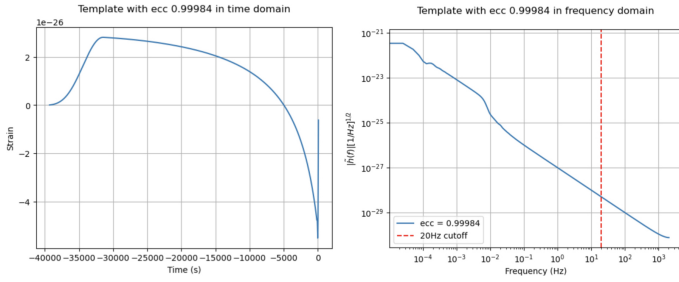
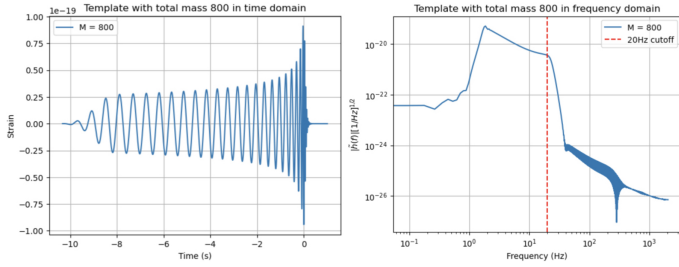
Figure 8. GWs waveform with $\varepsilon_0 = 0.99984$ in the time domain (left) and in the frequency domain (right).
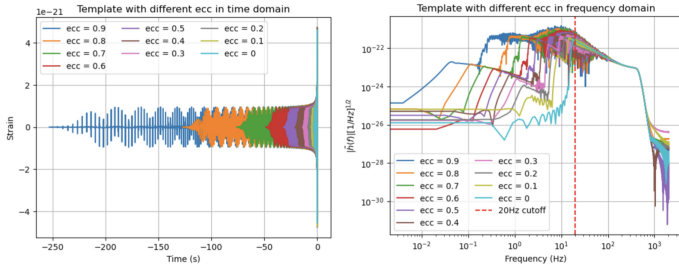

Figure 9. GWs waveform with different ε_0 in the time domain (left) and in the frequency domain (right).
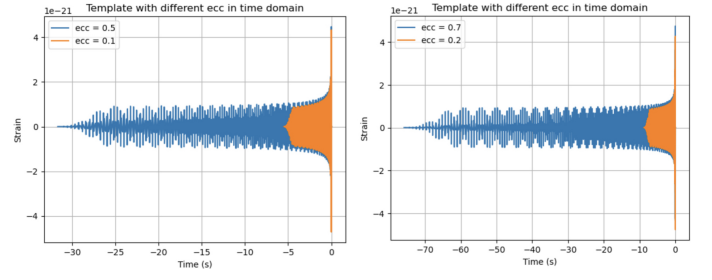
Figure 10. GWs waveform comparison between $\varepsilon_0 = 0.9$ and $\varepsilon_0 = 0.1$ (left) and between $\varepsilon_0 = 0.7$ and $\varepsilon_0 = 0.2$ (right).
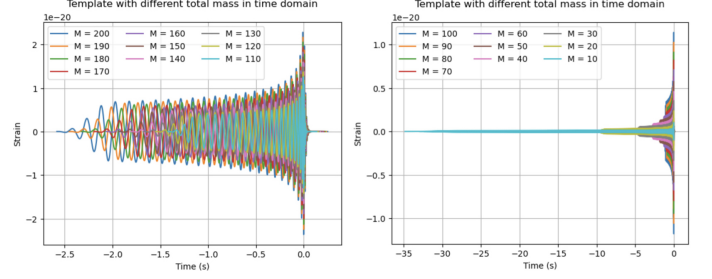
Figure 11. Waveforms in the time domain with $\varepsilon_0 = 0.0$ and total mass from $10 M_\odot$ to $100 M_\odot$ (left) and from $110 M_\odot$ to $200 M_\odot$ (right).
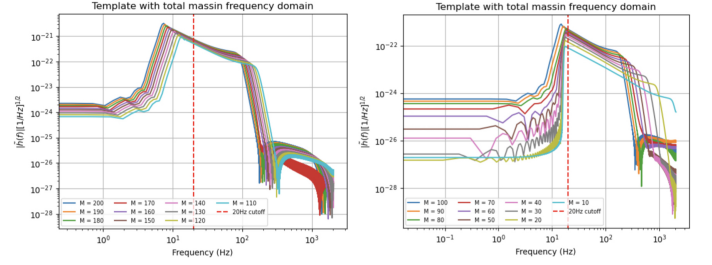
Figure 12. Waveforms in the frequency domain with $\varepsilon_0 = 0.0$ and total mass from $10 M_\odot$ to $100 M_\odot$ (left) and from $110 M_\odot$ to $200 M_\odot$ (right).
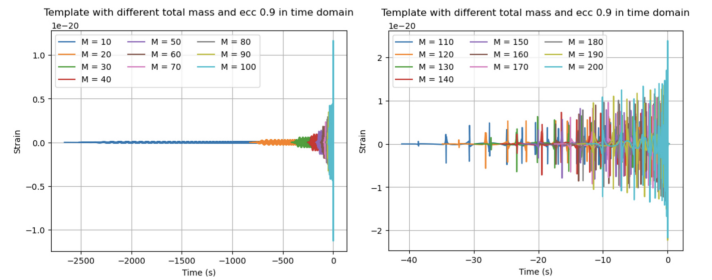
Figure 13. Waveforms in the time domain with $\varepsilon_0 = 0.9$ and total mass from $10 M_\odot$ to $100 M_\odot$ (left) and from $110 M_\odot$ to $200 M_\odot$ (right).
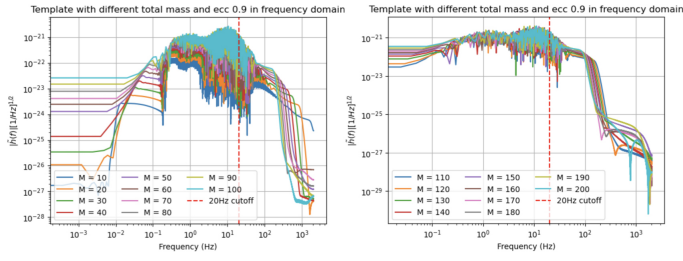
Figure 14. Waveforms in the frequency domain with $\varepsilon_0 = 0.9$ and total mass from 10M$_\odot$ to 100M$_\odot$ (left) and from 110M$_\odot$ to 200M$_\odot$ (right).
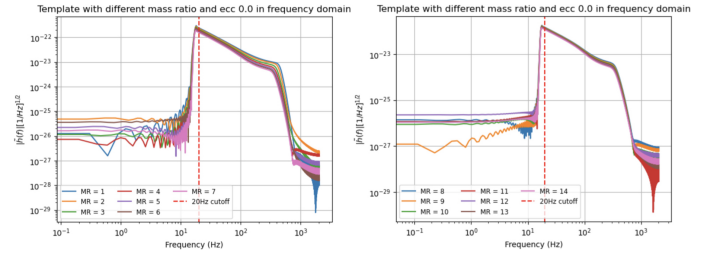
Figure 18. Waveforms in the frequency domain with $\varepsilon_0 = 0.0$ and mass ratio from 1 to 7 (left) and from 8 to 14 (right).

Figure 15. Waveforms with $\varepsilon_0 = 0.0$ and total mass 800M$_\odot$ in the time domain (left) and in the frequency domain (right).
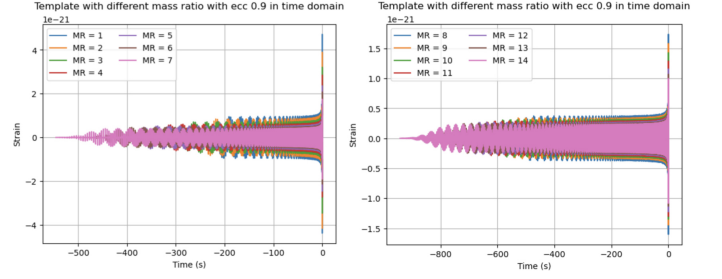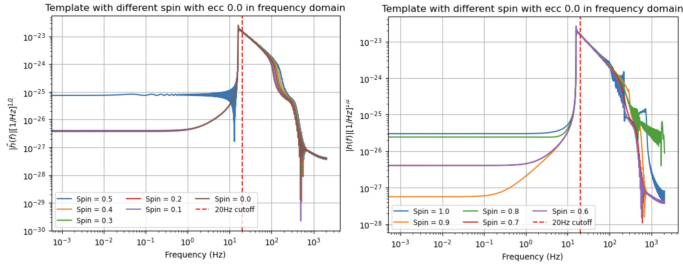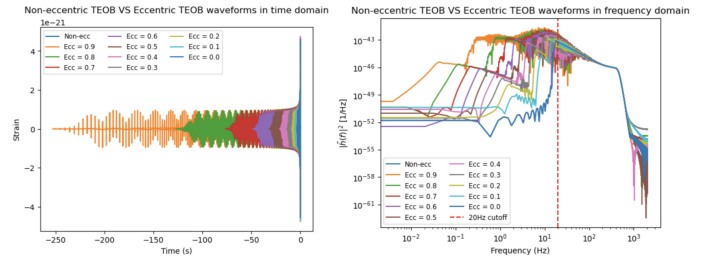

Figure 19. Waveforms in the time domain with $\varepsilon_0 = 0.9$ and mass ratio from 1 to 7 (left) and from 8 to 14 (right).
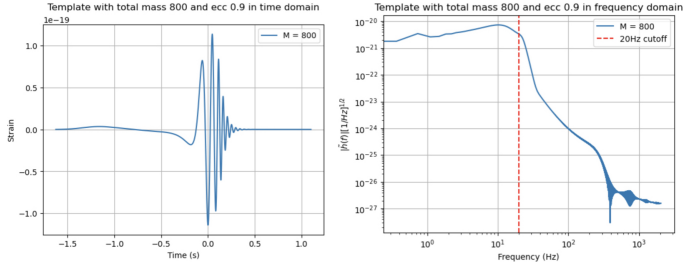
Figure 16. Waveforms with $\varepsilon_0 = 0.9$ and total mass 800M$_\odot$ in the time domain (left) and in the frequency domain (right).
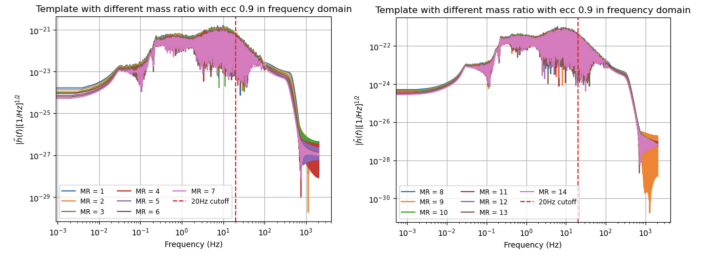
Figure 20. Waveforms in the time domain with $\varepsilon_0 = 0.9$ and mass ratio from 1 to 7 (left) and from 8 to 14 (right).
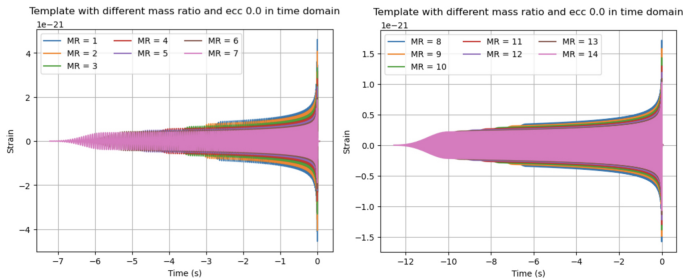
Figure 17. Waveforms in the time domain with $\varepsilon_0 = 0.0$ and mass ratio from 1 to 7 (left) and from 8 to 14 (right).
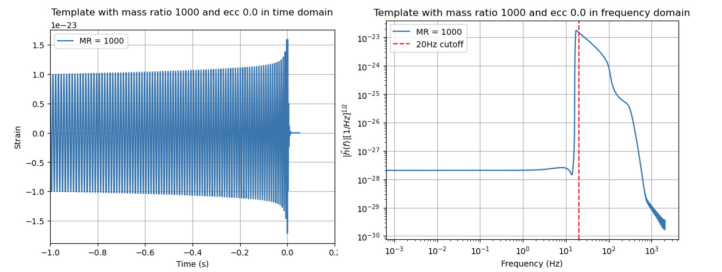
Figure 21. Waveforms with $\varepsilon_0 = 0.0$ and mass ratio 1000 in the time domain (left) and in the frequency domain (right).
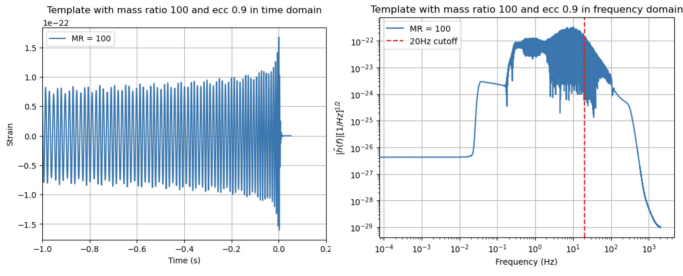
Figure 22. Waveforms with $\varepsilon_0 = 0.9$ and mass ratio 1000 in the time domain (left) and in the frequency domain (right).
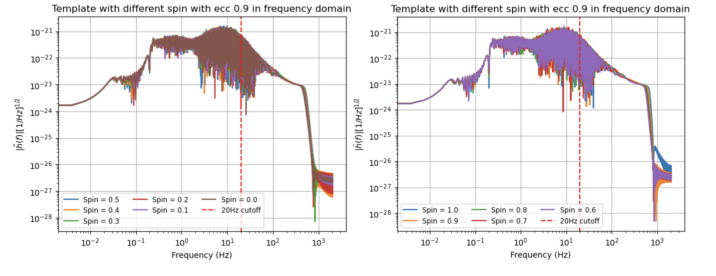
Figure 26. Waveforms in the frequency domain with $\varepsilon_0 = 0.9$ aligned-spin from 0.0 to 0.5 (left) and from 0.6 to 1.0 (right).
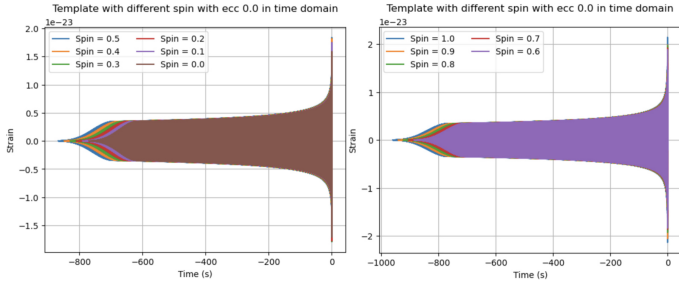
Figure 23. Waveforms in the time domain with $\varepsilon_0 = 0.0$ and aligned-spin from 0.0 to 0.5 (left) and from 0.6 to 1.0 (right).
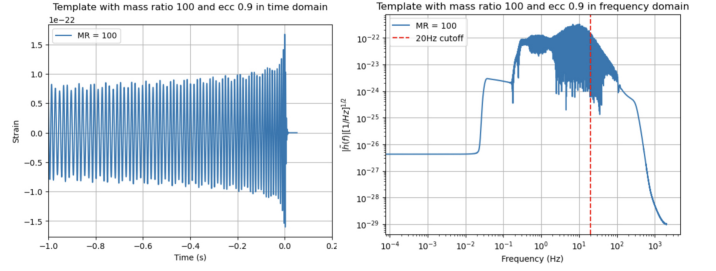
Figure 27. Waveforms with $\varepsilon_0 = 0.999$, mass ratio 100 and total mass $450M_\odot$ in the time domain (left) and in the frequency domain (right).

Figure 24. Waveforms in the frequency domain with $\varepsilon_0 = 0.0$ aligned-spin from 0.0 to 0.5 (left) and from 0.6 to 1.0 (right).

Figure 28. Eccentric TEOBResumS with different eccentricity and Non-eccentric TEOBResumS waveforms in the time domain (left) and frequency domain (right).
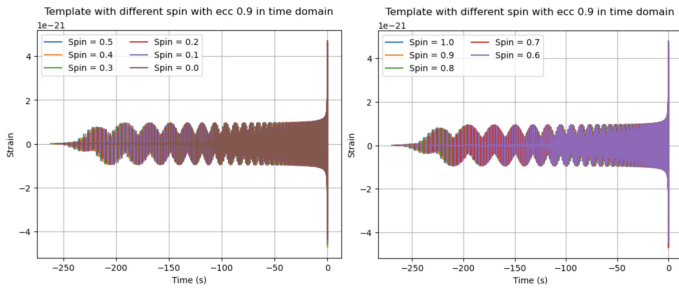
Figure 25. Waveforms in the time domain with $\varepsilon_0 = 0.9$ and aligned-spin from 0.0 to 0.5 (left) and from 0.6 to 1.0 (right).
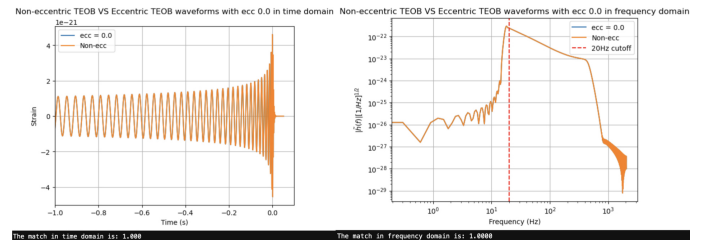
Figure 29. Eccentric TEOBResumS with $\varepsilon_0 = 0$ and Non-eccentric TEOBResumS waveforms with mass ratio 1 in the time domain (left) and frequency domain (right) with match values both 1.0.
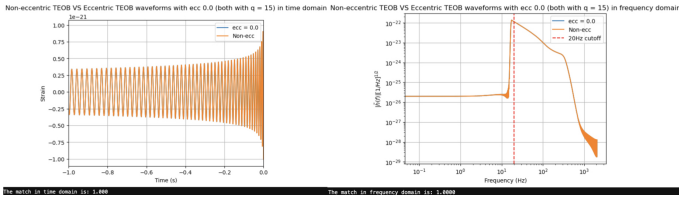
Figure 30. Eccentric TEOBResumS with $\varepsilon_0 = 0$ and Non-eccentric TEOBResumS waveforms with mass ratio 15 in the time domain (left) and frequency domain (right) with match values both 1.0.
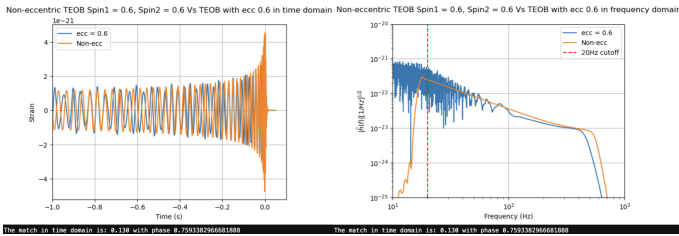

Figure 31. Eccentric TEOBResumS with $\varepsilon_0 = 0.2$ and aligned-spin TEOBResumS waveforms with spin 1 = 0.2 and spin 2 = 0.2 in the time domain (left) and frequency domain (right) with match values 0.507 and 0.156 respectively.
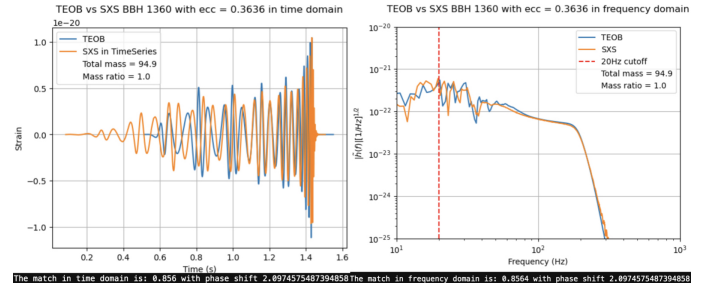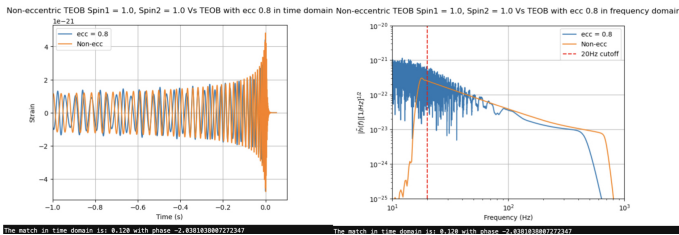

Figure 32. Eccentric TEOBResumS with $\varepsilon_0 = 0.6$ and aligned-spin TEOBResumS waveforms with spin 1 = 0.6 and spin 2 = 0.6 in the time domain (left) and frequency domain (right) with match values both 0.130.

Figure 33. Eccentric TEOBResumS with $\varepsilon_0 = 0.8$ and aligned-spin TEOBResumS waveforms with spin 1 = 1.0 and spin 2 = 1.0 in the time domain (left) and frequency domain (right) with match values both 0.120 respectively.

Figure 34. BBH 1569 from SXS and TEOBResumS waveforms with $\varepsilon_0 = 1.341 * 10^{-4}$ in the time domain (left) and frequency domain (right) with match values 0.953 and 0.9531 respectively.

Figure 35. BBH 1373 from SXS and TEOBResumS waveforms with $\varepsilon_0 = 0.2087$ in the time domain (left) and frequency domain (right) with match values 0.939 and 0.9386 respectively.

Figure 36. BBH 1360 from SXS and TEOBResumS waveforms with $\varepsilon_0 = 0.3636$ in the time domain (left) and frequency domain (right) with match values 0.856 and 0.8564 respectively.
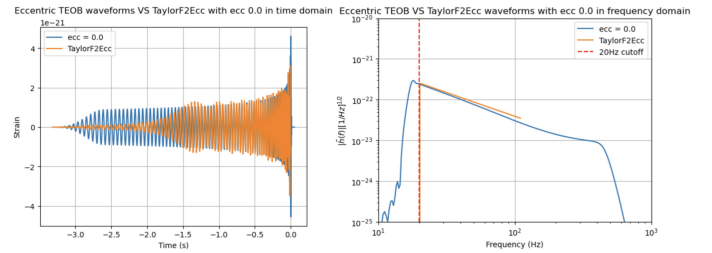

Figure 37. TaylorF2Ecc and TEOBResumS waveforms with $\varepsilon_0 = 0$ in the time domain (left) and frequency domain (right).
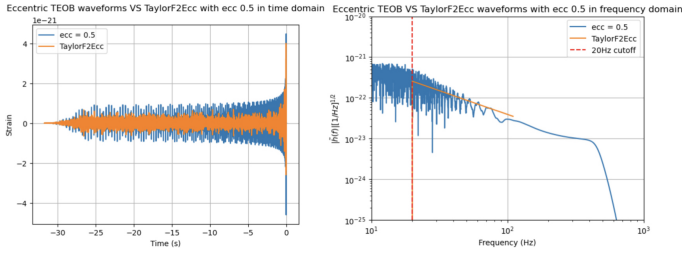
Figure 38. TaylorF2Ecc and TEOBResumS waveforms with $\varepsilon_0 = 0.5$ in the time domain (left) and frequency domain (right).
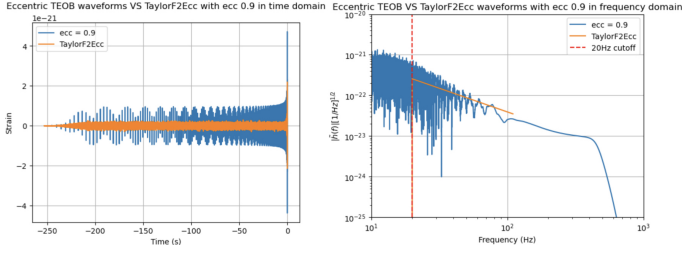

Figure 39. TaylorF2Ecc and TEOBResumS waveforms with $\varepsilon_0 = 0.9$ in the time domain (left) and frequency domain (right).
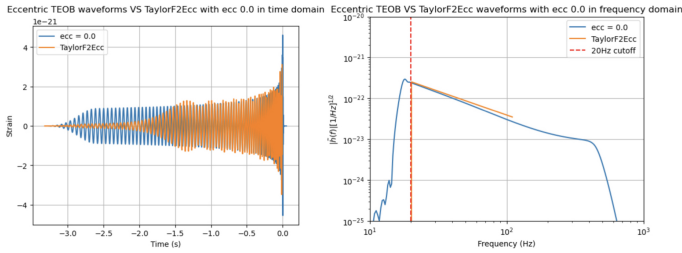

Figure 40. EccentricFD and TEOBResumS waveforms with $\varepsilon_0 = 0$ in the time domain (left) and frequency domain (right).
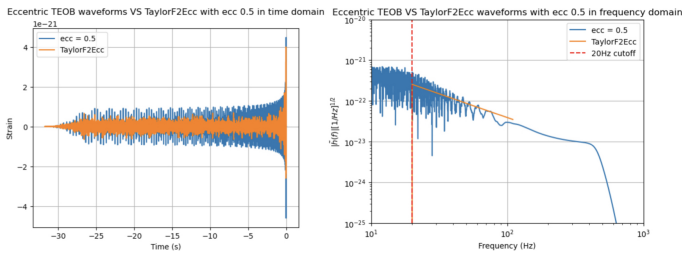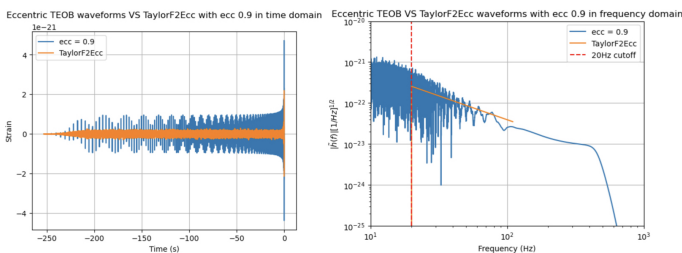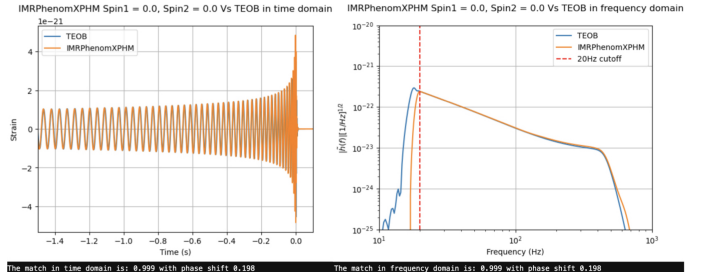

Figure 41. EccentricFD and TEOBResumS waveforms with $\varepsilon_0 = 0.5$ in the time domain (left) and frequency domain (right).

Figure 42. EccentricFD and TEOBResumS waveforms with $\varepsilon_0 = 0.9$ in the time domain (left) and frequency domain (right).

Figure 43. IMRPhenomXPHM and TEOBResumS waveforms with spin 1 and spin 2 equal 0.0 in the time domain (left) and frequency domain (right) with match values both 0.999.
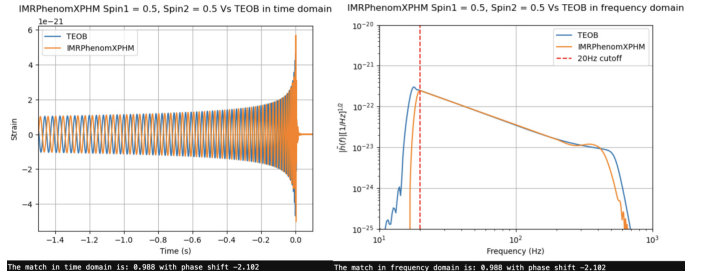

Figure 44. IMRPhenomXPHM and TEOBResumS waveforms with spin 1 and spin 2 equal 0.5 in the time domain (left) and frequency domain (right) with match values both 0.988.
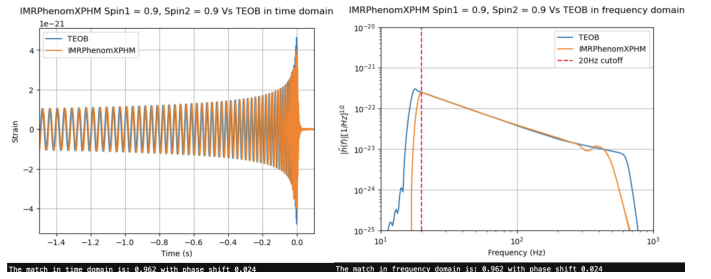

Figure 45. IMRPhenomXPHM and TEOBResumS waveforms with spin 1 and spin 2 equal 0.9 in the time domain (left) and frequency domain (right) with match values both 0.962.
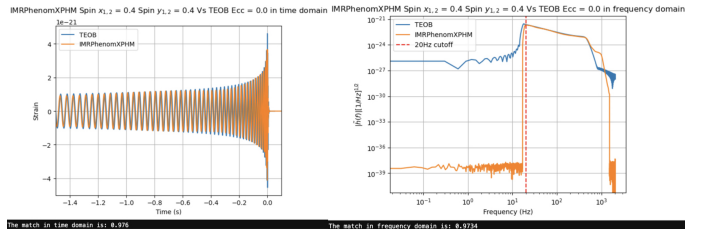

Figure 46. Eccentric TEOBResumS with $\varepsilon_0 = 0.0$ and precessing IMRPhenomXPHM waveforms with $S_x = 0.4$ and $S_y = 0.4$ in the time domain (left) and frequency domain (right) with match values 0.976 and 0.9734 respectively.
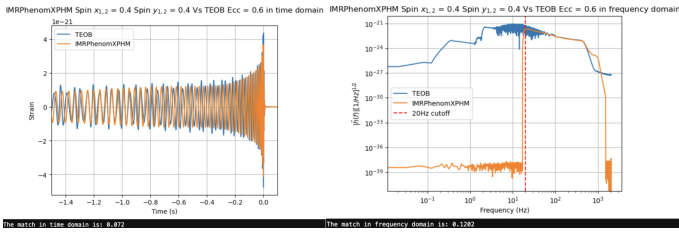
Figure 47. Eccentric TEOBResumS with $\varepsilon_0 = 0.6$ and precessing IMRPhenomXPHM waveforms with $S_x = 0.4$ and $S_y = 0.4$ in the time domain (left) and frequency domain (right) with match values 0.072 and 0.1202 respectively.
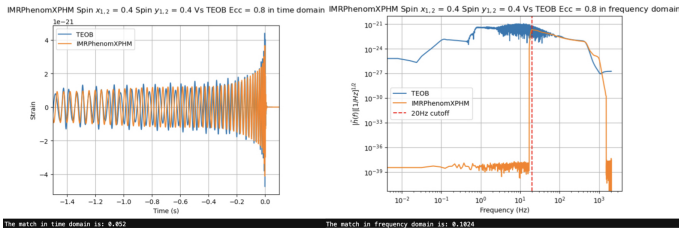
Figure 48. Eccentric TEOBResumS with $\varepsilon_0 = 0.8$ and precessing IMRPhenomXPHM waveforms with $S_x = 0.4$ and $S_y = 0.4$ in the time domain (left) and frequency domain (right) with match values 0.052 and 0.1024 respectively.
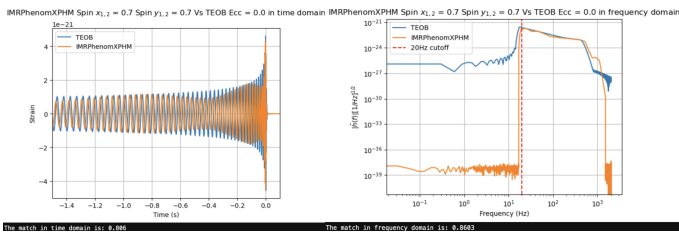
Figure 49. Eccentric TEOBResumS with $\varepsilon_0 = 0.0$ and precessing IMRPhenomXPHM waveforms with $S_x = 0.7$ and $S_y = 0.7$ in the time domain (left) and frequency domain (right) with match values 0.806 and 0.8603 respectively.
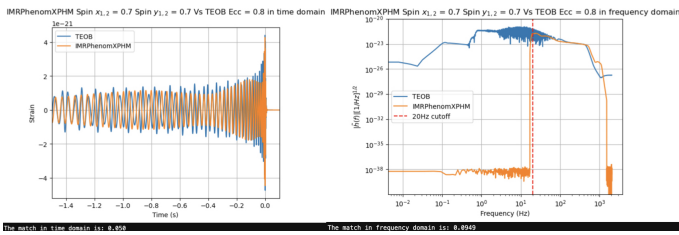
Figure 50. Eccentric TEOBResumS with $\varepsilon_0 = 0.8$ and precessing IMRPhenomXPHM waveforms with $S_x = 0.7$ and $S_y = 0.7$ in the time domain (left) and frequency domain (right) with match values 0.050 and 0.0949 respectively.
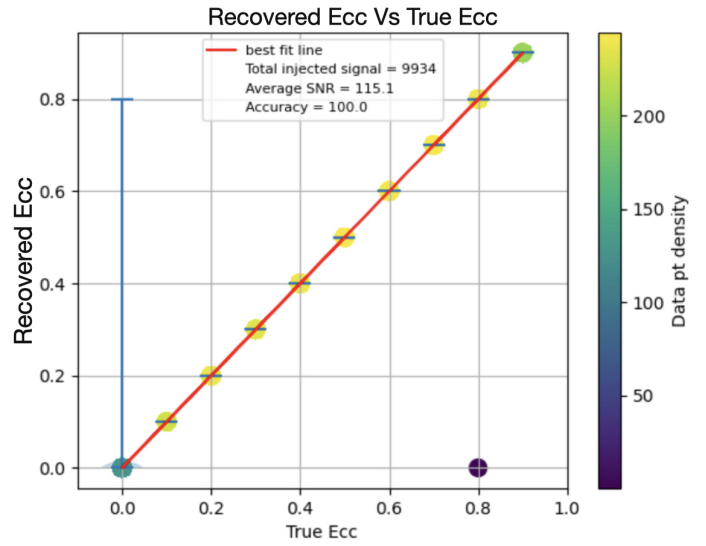
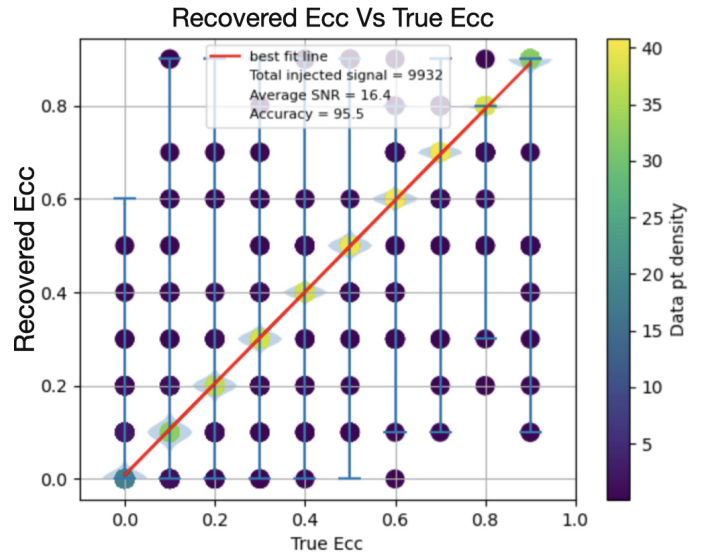Figure 51. Results by ENTRO with an average SNR of 100.

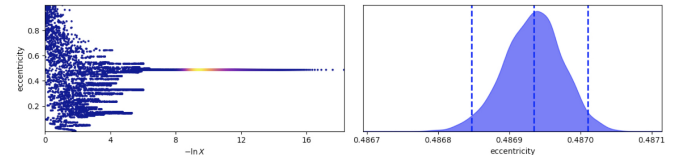Figure 52. Results by ENTRO with an average SNR of 15.

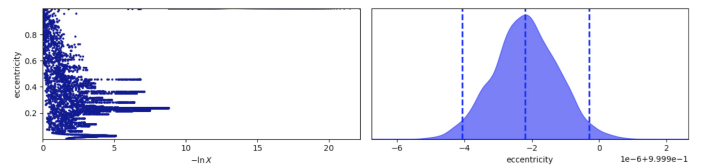Figure 53. Results by eENTRO precision 97.4%.

Figure 54. Results by eENTRO precision higher than 99.9%.

VIII. REFERENCES

[1] Indrajit Chakrabarty, "Gravitational waves: An introduction," (1999), arXiv:physics/9908041 [physics.ed-ph].

[2] Maurizio Spurio, "An introduction to astrophysical observables in gravitational wave detections," (2019), arXiv:1906.03643 [astro-ph.HE].

[3] Jan W. van Holten, "Curvature Dynamics in General Relativity," Universe 9, 110 (2023), arXiv:2211.10123 [gr-qc].

[4] M. Le Delliou, "Advanced General Relativity Notes," (2022) arXiv:2208.02506 [gr-qc].

[5] J. F. Pommaret, "General Relativity and Gauge Theory: Beyond the Mirror," arXiv e-prints , arXiv:2302.06585 (2023), arXiv:2302.06585 [math.GM].

[6] Gary Nash, "Modified General Relativity and dark matter," (2023), 10.1142/S0218271823500311, arXiv:2304.09671 [gr-qc].

[7] Maximiliano Isi, "Parametrizing gravitational-wave polarizations," (2022), arXiv:2208.03372 [gr-qc].

[8] R. Abbott et al. (KAGRA, VIRGO, LIGO Scientific), "Population of Merging Compact Binaries Inferred Using Gravitational Waves through GWTC-3," Phys. Rev. X 13, 011048 (2023), arXiv:2111.03634 [astro-ph.HE].

[9] J. Aasi et al. (LIGO Scientific), "Advanced LIGO," Class. Quant. Grav. 32, 074001 (2015), arXiv:1411.4547 [gr-qc].

[10] F. Acernese et al. (VIRGO), "Advanced Virgo: a second-generation interferometric gravitational wave detector," Class. Quant. Grav. 32, 024001 (2015), arXiv:1408.3978 [gr-qc].

[11] Kentaro Somiya (KAGRA), "Detector configuration of KAGRA: The Japanese cryogenic gravitational-wave detector," Class. Quant. Grav. 29, 124007 (2012), arXiv:1111.7185 [gr-qc].

[12] B. P. Abbott et al. (LIGO Scientific, Virgo), "GWTC-1: A Gravitational-Wave Transient Catalog of Compact Binary Mergers Observed by LIGO and Virgo during the First and Second Observing Runs," Phys. Rev. X 9, 031040 (2019), arXiv:1811.12907 [astro-ph.HE].

[13] R. Abbott et al. (LIGO Scientific, Virgo), "GWTC-2: Compact Binary Coalescences Observed by LIGO and Virgo During the First Half of the Third Observing Run," Phys. Rev. X 11, 021053 (2021), arXiv:2010.14527 [gr-qc].

[14] R. Abbott et al. (LIGO Scientific, VIRGO, KAGRA), "GWTC-3: Compact Binary Coalescences Observed by LIGO and Virgo During the Second Part of the Third Observing Run," (2021), arXiv:2111.03606 [gr-qc].

[15] B. P. Abbott et al. (LIGO Scientific, Virgo), "Search for Eccentric Binary Black Hole Mergers with Advanced LIGO and Advanced Virgo during their First and Second Observing Runs," Astrophys. J. 883, 149 (2019), arXiv:1907.09384 [astro-ph.HE].

[16] Tao Yang, Rong-Gen Cai, Zhoujian Cao, and Hyung Mok Lee, "Parameter estimation of eccentric gravitational waves with a decihertz observatory and its cosmological implications," Phys. Rev. D 107, 043539 (2023), arXiv:2212.11131 [gr-qc].

[17] Stefano Schmidt, Bhooshan Gadre, and Sarah Caudill, "Gravitational-wave template banks for novel compact binaries," (2023), arXiv:2302.00436 [gr-qc].

[18] Michela Mapelli, "Binary Black Hole Mergers: Formation and Populations," Front. Astron. Space Sci. 7, 38 (2020), arXiv:2105.12455 [astro-ph.HE].

[19] Bruce Allen, Warren G. Anderson, Patrick R. Brady, Duncan A. Brown, and Jolien D. E. Creighton, "FINDCHIRP: An Algorithm for detection of gravitational waves from inspiraling compact binaries," Phys. Rev. D 85, 122006 (2012), arXiv:gr-qc/0509116.

[20] Koustav Chandra, V. Villa-Ortega, T. Dent, C. McIsaac, Archana Pai, I. W. Harry, G. S. Cabourn Davies, and K. Soni, "An optimized PyCBC search for gravitational waves from intermediate-mass black hole mergers," Phys. Rev. D 104, 042004 (2021), arXiv:2106.00193 [gr-qc].

[21] Samantha A. Usman et al., "The PyCBC search for gravitational waves from compact binary coalescence," Class. Quant. Grav. 33, 215004 (2016), arXiv:1508.02357 [gr-qc].

[22] Derek Davis, Max Trevor, Simone Mozzon, and Laura K. Nuttall, "Incorporating information from LIGO data quality streams into the PyCBC search for gravitational waves," Phys. Rev. D 106, 102006 (2022), arXiv:2204.03091 [gr-qc].

[23] Gregory Ashton et al., "BILBY: A user-friendly Bayesian inference library for gravitational-wave astronomy," Astrophys. J. Suppl. 241, 27 (2019), arXiv:1811.02042 [astro-ph.IM].

[24] Nelson Christensen and Renate Meyer, "Parameter estimation with gravitational waves," Rev. Mod. Phys. 94, 025001 (2022), arXiv:2204.04449 [gr-qc].

[25] Gregory Ashton and Colm Talbot, "B ilby-MCMC: an MCMC sampler for gravitational-wave inference," Mon. Not. Roy. Astron. Soc. 507, 2037–2051 (2021), arXiv:2106.08730 [gr-qc].

[26] P. C. Peters, "Gravitational radiation and the motion of two point masses," Phys. Rev. 136, B1224–B1232 (1964).

[27] E. A. Huerta, Prayush Kumar, Sean T. McWilliams, Richard O'Shaughnessy, and Nicolás Yunes, "Accurate and efficient waveforms for compact binaries on eccentric orbits," Phys. Rev. D 90, 084016 (2014), arXiv:1408.3406 [gr-qc].

[28] Sashwat Tanay, Maria Haney, and Achamveedu Gopakumar, "Frequency and time domain inspiral templates for comparable mass compact binaries in eccentric orbits," Phys. Rev. D 93, 064031 (2016), arXiv:1602.03081 [gr-qc].

[29] Soichiro Isoyama, Riccardo Sturani, and Hiroyuki Nakano, "Post-Newtonian templates for gravitational waves from compact binary inspirals," (2020), 10.1007/978-981-15-4702-7_31 − 1, arXiv:2012.01350 [gr-qc].

[30] Danilo Chiaramello and Alessandro Nagar, "Faithful analytical effective-one-body waveform model for spin-aligned, moderately eccentric, coalescing black hole binaries," Phys. Rev. D 101, 101501 (2020), arXiv:2001.11736 [gr-qc].

[31] Abhishek V. Joshi, Shawn G. Rosofsky, Roland Haas, and E. A. Huerta, "Numerical relativity higher order gravitational waveforms of eccentric, spinning, nonprecessing binary black hole mergers," Phys. Rev. D 107, 064038 (2023), arXiv:2210.01852 [gr-qc].